Supporting Information

Quantitative single-molecule study reveals site-specific photo-oxidation activities and kinetics on 2D g-C_3N_4

Shuyang Wu,† Jenica Marie L. Madridejos,† Jinn-Kye Lee, Rong Xu, Yunpeng Lu, Zhengyang Zhang**

School of Chemistry, Chemical Engineering and Biotechnology, Nanyang Technological University, 21 Nanyang Link, Singapore 637371.

Corresponding Author

E-mail: yplu@ntu.edu.sg

E-mail: zhang.zy@ntu.edu.sg

†These authors contributed equally.

Section 1. Experimental section

Synthesis of the photocatalysts

The g-C_3N_4 was prepared through thermal polymerization of melamine followed by subsequent thermal exfoliation in air.[1] In a typical preparation, 5 g of melamine was put into a covered crucible and then heated to 500 ^oC for 2 h with a rate of 2 ^oC min^{-1}. Next, the calcination temperature was increased to 520 ^oC and maintained for 2 h. The yellow product was ground and 1 g of the product was put in an ark. The powder was evenly spread to a thin layer and put in the muffle furnace. Then it was heated to 520 ^oC with a ramping rate of 2 ^oC min^{-1} and maintained for 6 h. The obtained white product was named as CNS.

Materials characterization

Transmission electron microscopy (TEM) was conducted on JEOL JEM-2100Plus microscope. Atomic-force microscopy (AFM) images were obtained on Bruker Dimension XR Icon AFM. The X-ray diffraction (XRD) pattern was acquired on Bruker D2 Phaser diffractometer with Cu Kα irradiation (λ=1.54184 Å) at 10 mA and 30 kV as the incident beam. Fourier transform infrared (FTIR) spectroscopy was carried out on Perkin-Elmer spectrophotometer (Spectrum 100). Ultraviolet photoelectron spectroscopy (UPS) was conducted on Shimadzu Kratos Axis Supra spectrometer equipped with He-I photon source (21.21 eV). UV-vis diffuse reflection spectra (DRS) were collected on the Shimadzu UV-2450 spectrophotometer.

Single-molecule fluorescence imaging

The SMF imaging was performed on a total internal reflection fluorescence (TIRF) microscope (Nikon Eclipse Ti-U). In a typical preparation of sample-deposited coverslip, a few drops of catalyst ink (1 mg mL^{-1}) were deposited on the coverslip and fully dried in the oven. Then, a microflow chamber (75.5 mm × 25.5 mm × 0.6 mm) was attached to the coverslip and sealed

tightly, which was transferred and fixed on the microscope stage. The Amplex® red (AR) solution was bubbled with N_2 gas for 30 min to remove O_2 in the solution before introduced to the reaction chamber. Different concentrations of AR (0.02, 0.05, 0.1, 0.2, 0.5 and 1 μM) solutions were pumped to the chamber with a flowrate of 20 μL min^{-1}. The brightfield images were collected before illumination. The photocatalyst and resorufin were excited by a circularly polarized 405 nm laser (5 mW, L6CC Oxxius) and a 532 nm laser (20 mW), respectively through a quad-edge laser dichroic mirror (Di03-R405/488/532/635-t1-25x36, Semrock). The photoluminescence (PL) signal passed through oil-immersion objective lens (Nikon Plan Apo λ 100×, NA 1.45) and a band-pass filter (ET605/70m, Chroma) to reduce the photocatalyst PL signal. Then, the signal was collected by a high-speed electron multiplying charge coupled device (EMCCD) camera (Andor iXon3, 60 Hz). In a typical run, a video composed of more than 30000 frames was recorded and finally processed by the software.

Computational details

To provide further insights into the photocatalytic activities of different g-C_3N_4 surfaces, DFT calculations with Vienna Ab-initio Simulation Package (VASP)[2-5] were performed for the adsorption of AR on BP, wrinkle, and edge. In our calculations, the Perdew-Burke-Ernzerhof (PBE)[6, 7] functional of the generalized gradient approximation with a plane-wave cut-off energy of 450 eV was used.[8, 9] The basal plane and wrinkle surfaces were based on previous work on g-C_3N_4 while the edge was modelled by terminating the N-atoms with hydrogen and adding 10 Å to signify the end of the surface. Optimization calculations were performed using energy and force convergence limits equal to 10^{-4} eV per atom and 0.01 eV $Å^{-1}$ for different surface slabs with explicit dispersion corrections using D3 Grimme's method (DFT-D3).[10, 11] Geometric constraints were applied to both BP and edge g-C_3N_4 surfaces to prevent their corrugation into the more stable

wrinkle structures. The Brillouin zone integration was carried out with a 3 × 3 × 1 Monkhorst-Pack grid for the different surface slabs, and the vacuum height was set to 20 Å between different layers. To optimize AR, the unit cell is set to 20 Å × 20 Å × 20 Å to avoid interactions between neighboring molecules and a 1 × 1 × 1 Monkhorst-Pack grid. Several initial locations and configurations of AR on all three surfaces were considered based on symmetry and other important molecular interactions. All the input geometries were optimized and reported in the Supporting Information while the most stable structures in energy are presented here. The adsorption energy (E_{ads}) was calculated according to **Eqn. S1**

$$E_{ads} = -(E_{total} - E_{substrate} - E_{gas-phase\ adsorbate}) \quad \text{(S1)}$$

Where E_{total} is the total energy calculated for the substrate with adsorbed reactant or product, $E_{substrate}$ is the calculated energy of the clean substrate, and $E_{gas-phase\ adsorbate}$ is the calculated energy of adsorbed gas phase molecule. To elucidate further the interactions between the adsorbate and substrate, the change of charge densities was quantified using Bader charge analysis.[12-14]

Section S2. Morphology and physicochemical properties of CNS.

The phase structure of CNS was characterized by XRD as shown in **Fig. S1a**. The (002) plane of g-C_3N_4 is identified by the diffraction peak at 27.5°, which is attributed to the interplanar periodic stacking of aromatic rings.[15] The low-angle peak at around 13° which is related to the in-plane packing of tri-s-triazine motifs is absent in our result. This is probably due to the decrease of planar size during the thermal etching process. FTIR spectra were collected to further verify the CNS structure (**Fig. S1b**). The broad band between 3000 and 3600 cm^{-1} is ascribed to the stretching mode of N-H bonds. The peaks in the range of 1100 and 1650 cm^{-1} correspond to the aromatic heterocycle stretching.[16] The vibrational bending of triazine rings accounts for the absorption peak at 808 cm^{-1}.[17] The morphology and structural features of CNS are revealed in the TEM images. In **Fig. S2a**, CNS exhibits an ultrathin and graphene-like structure with great tunability and flexibility. The thickness is measured to be ~9.5 nm by AFM (**Fig. S3**). The rough surface of CNS is observed, which is caused by the decomposition of polymeric melon units in the g-C_3N_4 planar structure.[18] Besides, the wrinkle structure is formed by folding or bending of BPs (**Fig. S2a,b**), which reduces the surface energy of CNS. UV-vis DRS and UPS spectra were recorded to study the optical properties of CNS. In **Fig. S2c**, the bandgap energy of CNS is determined to be 3.0 eV by the Tauc plot (inset of **Fig. S2c**). The slight enhanced absorption in the visible light region is probably due to the multiple scattering effect caused by the porous nature of CNS.[19] The valence band (VB) potential of CNS was determined by UPS. As shown in **Fig. S2d**, the VB maximum is determined to be 1.85 eV and thus the conduction band (CB) minimum of CNS is calculated to be -1.15 eV (inset of **Fig. S2d**). The relative positive VB position of CNS provides sufficient oxidation potential for compound photodegradation, which contributes to the pollutant removal and environmental purification.

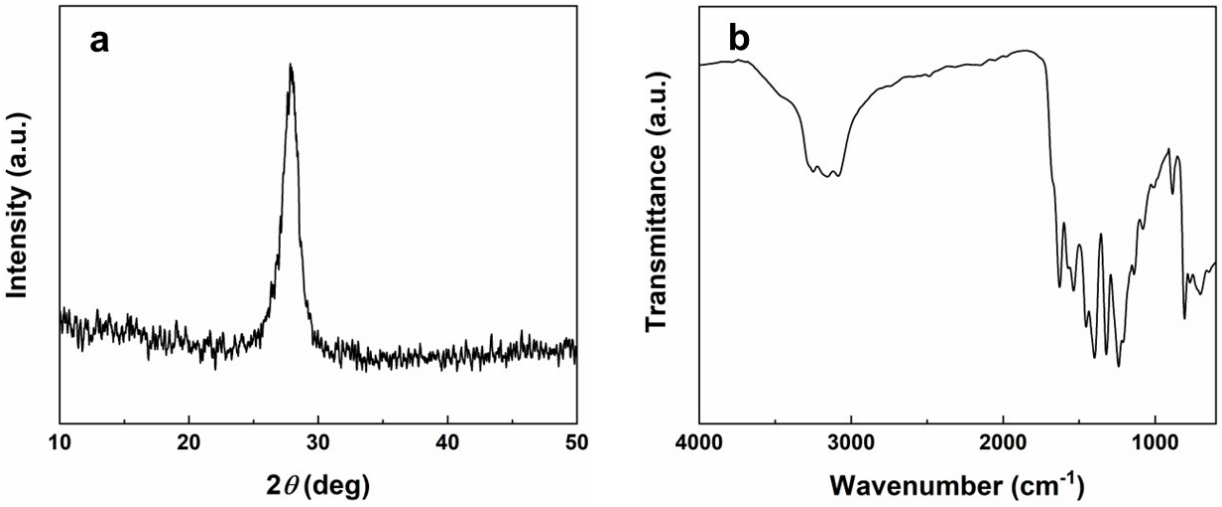

Fig. S1 (a) XRD patterns and (b) FTIR spectra of CNS.

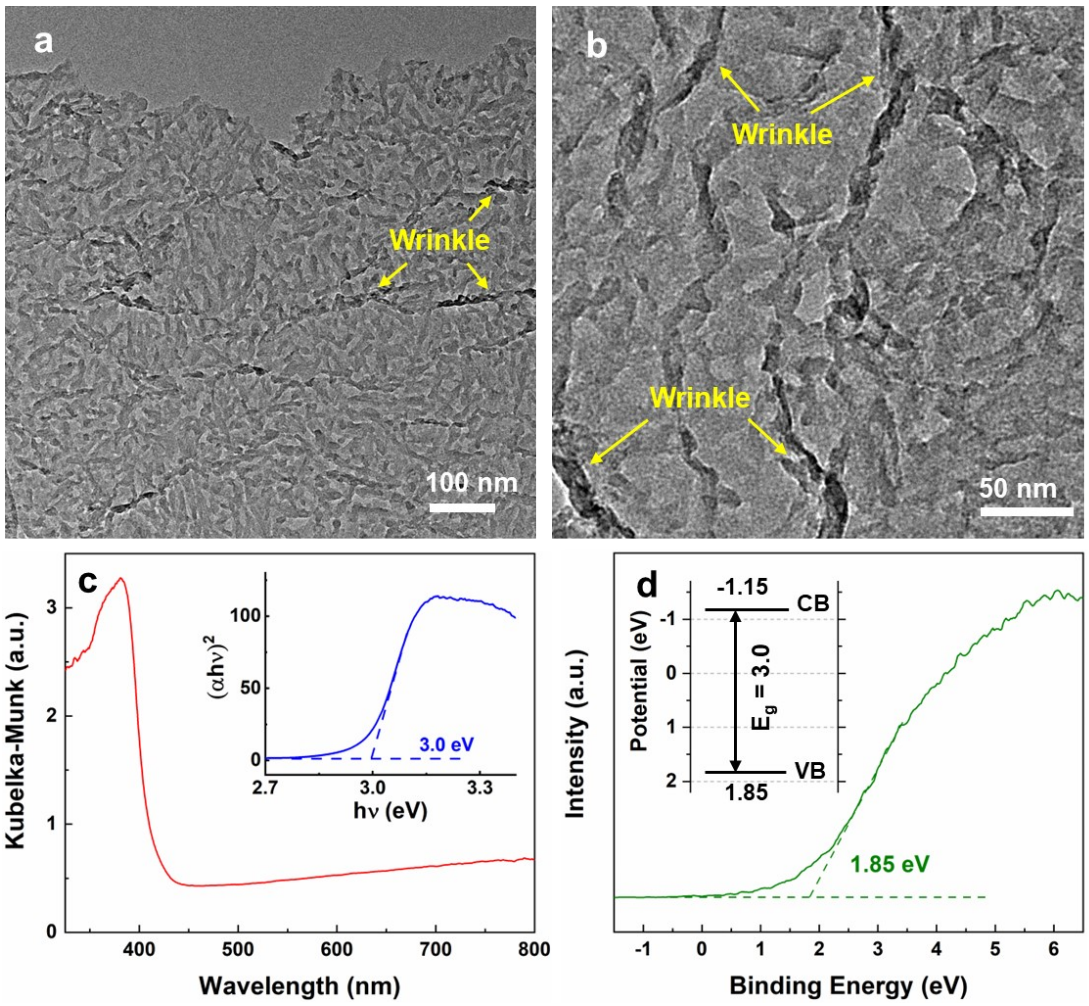

Fig. S2 Morphology and optical properties of CNS. (a, b) TEM images, (c) UV-vis DRS spectra (inset: Tauc plot) and (d) UPS spectra (inset: energy level diagram for bandgap analysis) of CNS.

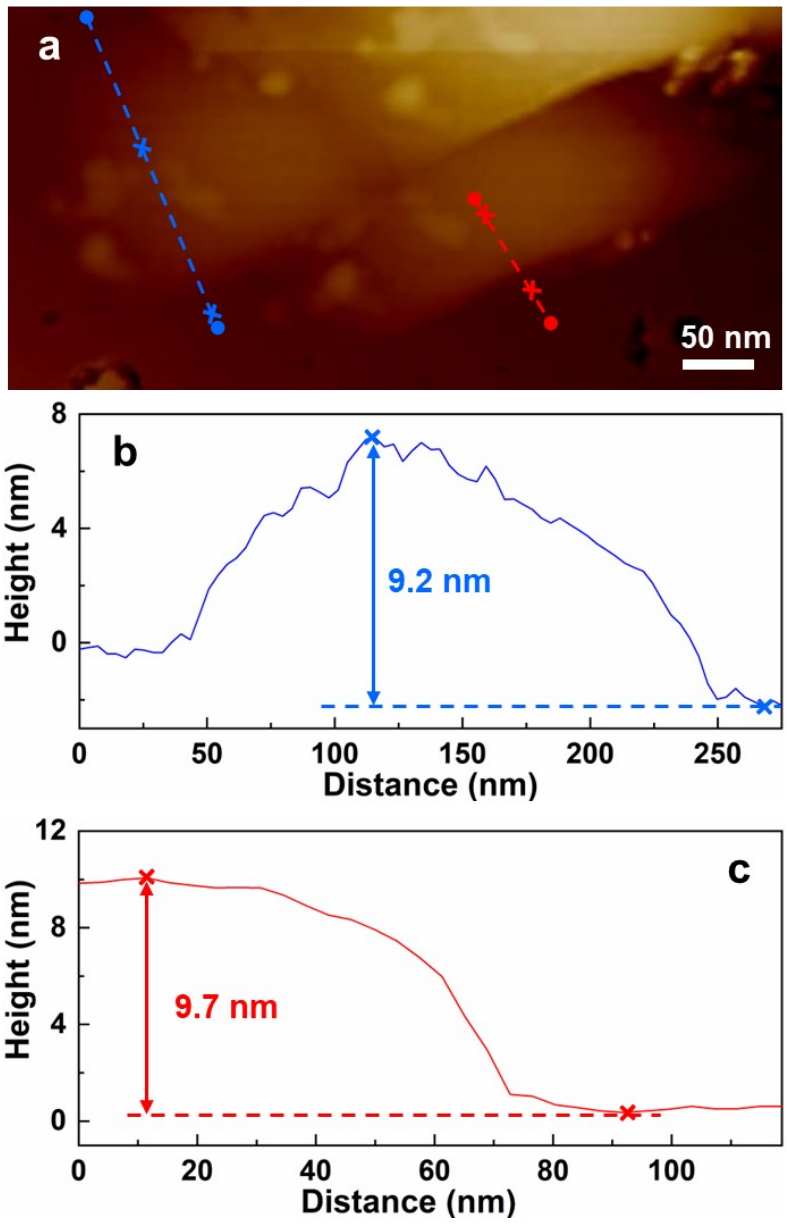

Fig. S3 (a) AFM images and (b, c) height curves of CNS.

Section S3. SMF study of site-specific catalytic activities, dynamics.

The non-fluorescent AR was used as probe molecules to detect h^+ and study the catalytic heterogeneities on wrinkles, edges and BPs of CNS (**Fig. S4**). The kinetic steps including reactant absorption, conversion, product dissociation and temporal activity fluctuations are quantified on such structures. Upon laser excitation (405 nm), AR can be photo-oxidized via an indirect way by •OH radicals produced from the reaction of h^+ and OH^- in water.[20] The product molecule, resorufin is photoexcited by the 532 nm laser and the emitted fluorescence signal is collected by the EMCCD camera with high sensitivity. Hence, in **Fig. S5a**, the bright dots (in yellow circles) represent the formation of fluorescent resorufin molecules on CNS.

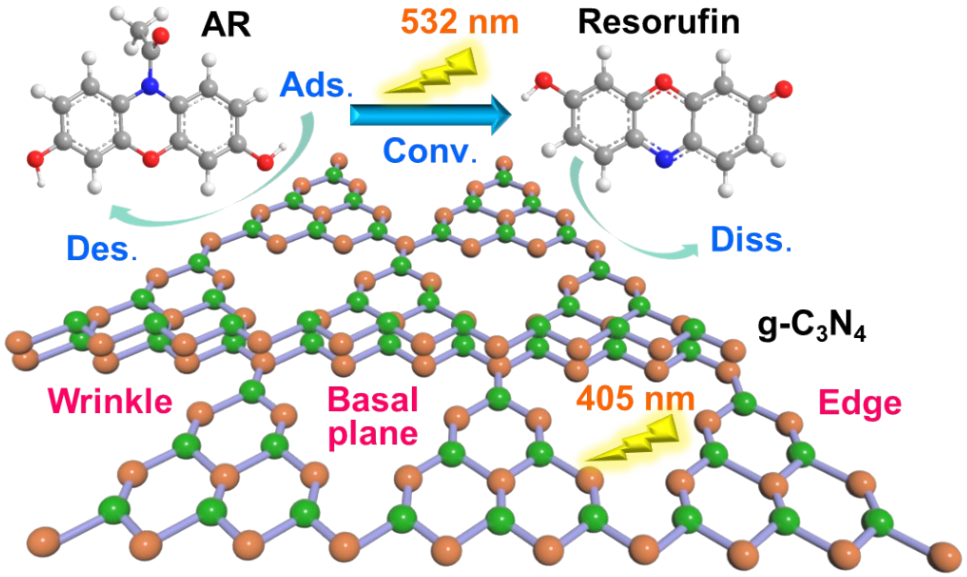

Fig. S4 Schematic of the photocatalytic process under the TIRF microscope.

131 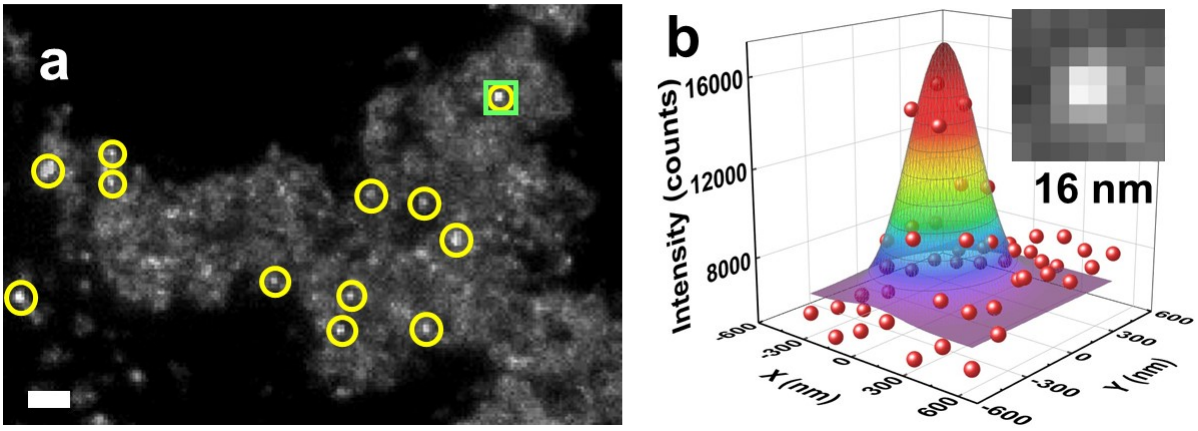

132 **Fig. S5** (a) A single frame of fluorescent bursts (in yellow circles) on CNS. (b) The calculation of

133 spatial resolution using 2D Gaussian fitting (inset: the area from the green square in (a)).

134

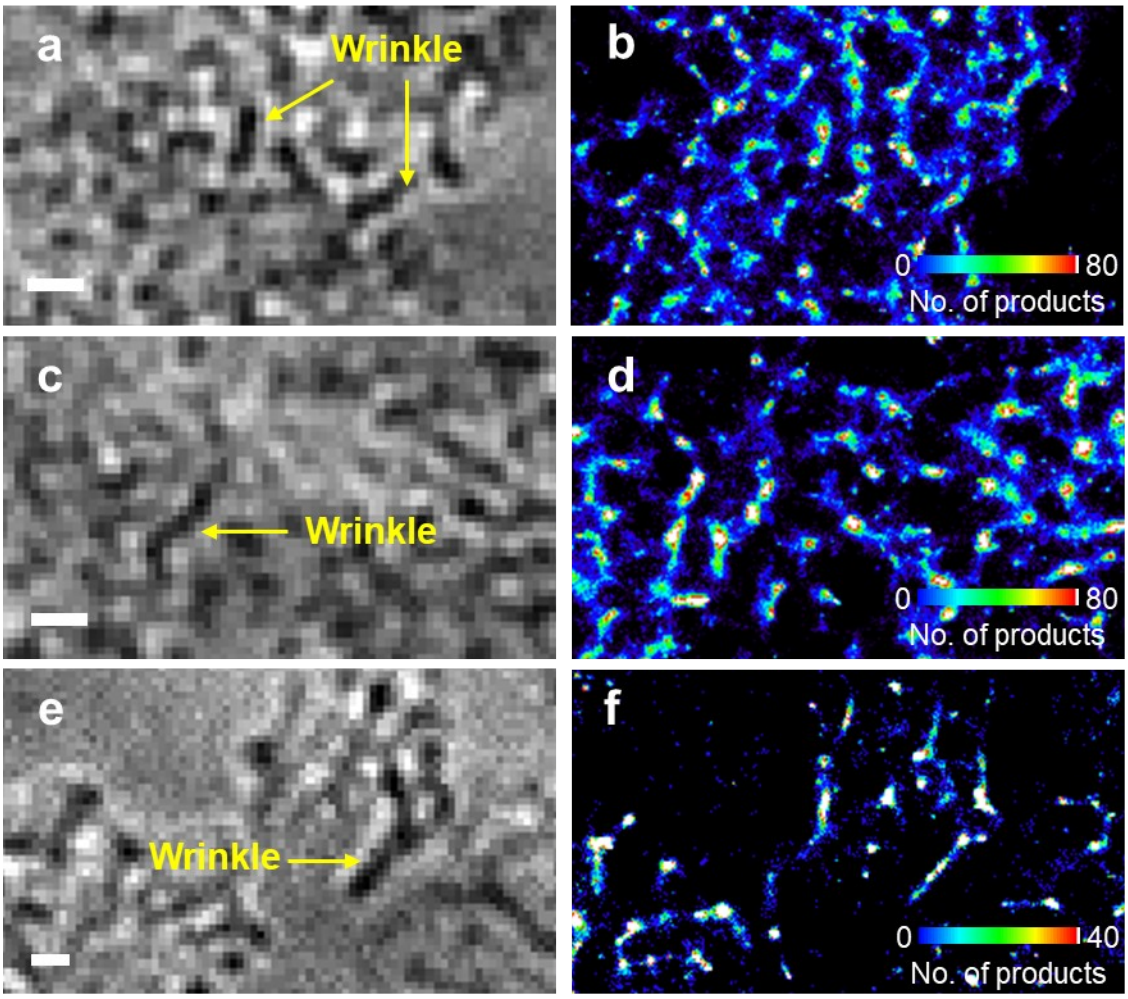

Fig. S6 (a, c, e) The bright-field images and (b, d, f) corresponding density maps (bin size: 30 nm × 30 nm) of CNS with AR. Scale bar: 1 μm.

Section S4. Determine the localization precision of SMF imaging.

Based on the previous works,[21, 22] the localization precision can be determined by fitting the fluorescence intensity with 2D elliptical Gaussian functions (**Eqn. S2, Fig. S5b**):

$$I(x,y) = A + B * exp(-(\frac{(x-x_0)^2}{2S_x^2} + \frac{(y-y_0)^2}{2S_y^2})) \quad \text{(S2)}$$

where (x_0, y_0) is the center position, A is the background level, B is the peak intensity at (x_0, y_0), S_x and S_y are the standard deviations of the Gaussian distribution along the x- and y-axes, respectively. The localization precision (σ_j, $_{j=x, y}$) can be calculated using **Eqn. S3**:

$$\sigma_j = \sqrt{(\frac{S_j^2}{N} + \frac{a^2/12}{N} + \frac{8\pi S_j^4 b^2}{a^2 N^2})} \quad \text{(S3)}$$

where N is the photons collected, a is the pixel size, and b is the background noise in photons. For the fluorescent burst in the inset of **Fig. S5b**, the parameters are calculated to be S_x = 143 nm, S_y = 164 nm, a = 160 nm, N = 660, b = 13, σ_x =14 nm and σ_y =18 nm. Thus, the average localization precision is calculated to be σ_{xy} = 16 nm using **Eqn. S4**:

$$\sigma_{xy} = (\sigma_x + \sigma_y)/2 \quad \text{(S4)}$$

Section S5. Image segmentation.

To determine the size of reaction subregions, image segmentation was carried out. As shown in **Fig. S7b,c**, the cross-profiles on the wrinkle and edge are obtained from the marked rectangles in **Fig. S7a**. The intensity-position profiles are fitted with Gaussian function to obtain the FWHM. The averaged FWHM for the wrinkle and edge profiles are determined to be 164 and 154 nm, respectively (**Table S1**). Such values are close to the size of one pixel (160 nm). Thus, the sizes of the subregions for wrinkles and edges are 1×1 pixel (160 nm × 160 nm). Besides, we make sure that each subregion contains one fluorescent burst. Otherwise, the size along the wrinkle or edge is reduced (e.g., 100 nm × 160 nm) to meet this criterion. Regarding the BPs, we also use the subregion size of 160 nm × 160 nm for convenience with one fluorescent burst in a subregion.

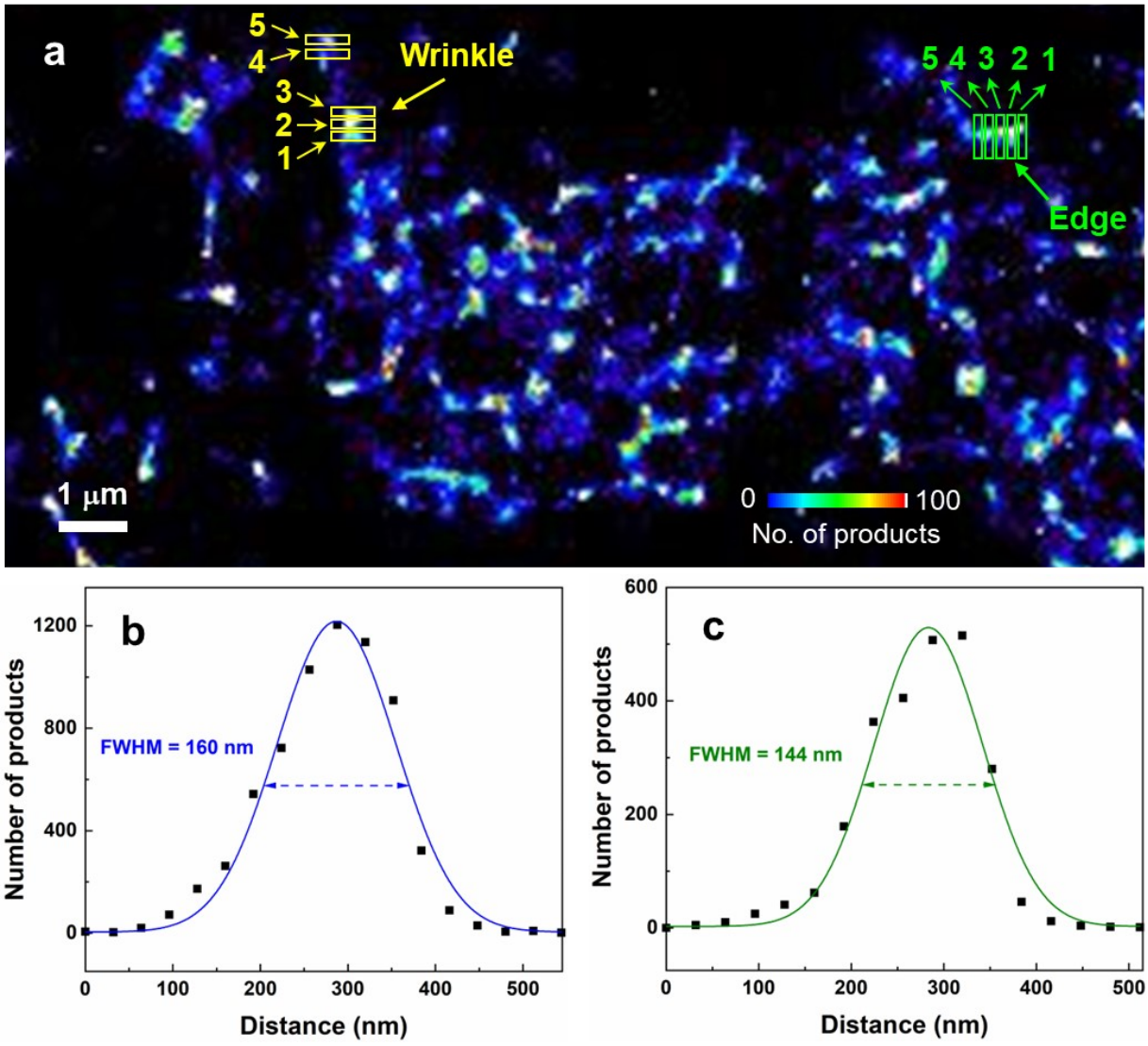

Fig. S7 (a) Image segmentation of wrinkles and edges in the density map. Cross-profiles of number of products fitted by Gaussian function at the (b) wrinkle (position 2) and (c) edge (position 3) marked in (a).

Table S1. The FWHM of cross-profiles of number of products at wrinkle and edge positions.

Positions	1	2	3	4	5	Average
Wrinkle FWHM (nm)	198	160	178	137	145	164
Edge FWHM (nm)	130	186	144	158	151	154

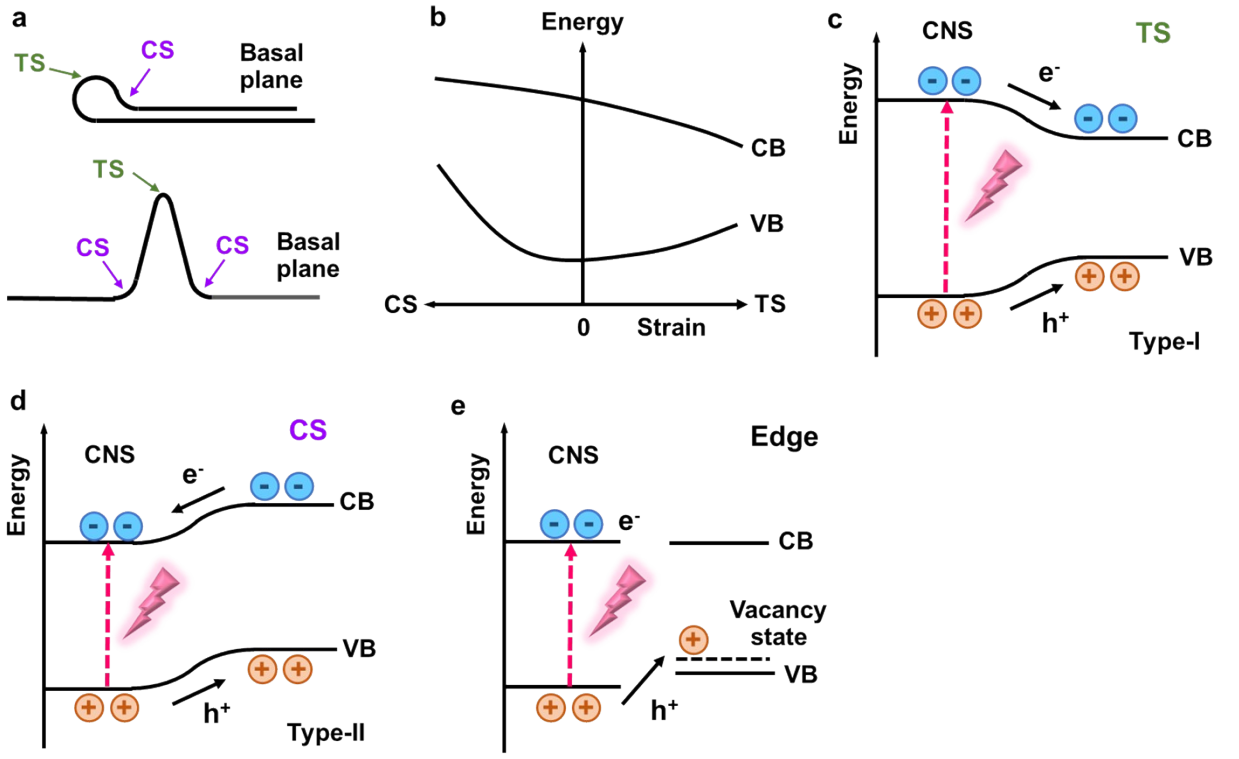

Fig. S8 (a) Schematic of wrinkle formation and strain distributions in wrinkles. (b) The dependence of CB and VB positions on the CS and TS present in the structure. Schematic of band modulation with presence of (c) TS in wrinkles, (d) CS in wrinkles and (e) vacancies in edges.

Section S6. SMF study of temporal activity fluctuations.

To study the temporal variation of reaction rates, the number of single turnovers per unit time (turnover rates) was analyzed based on the trajectories (**Fig. S9a**). The activity fluctuation is related to the perturbation in chemical reaction (τ_{off}), product dissociation (τ_{on}) or both, known as catalysis-induced activity fluctuations.[23] The autocorrelation functions, $C_\tau(m) = \langle \Delta\tau(0)\Delta\tau(m)\rangle / \langle \Delta\tau(0)^2 \rangle$, can be used to analyze the effect of τ_{off} and τ_{on} on fluctuations, where $\Delta\tau(m) = \tau(m) - \langle\tau\rangle$, τ represent τ_{off} or τ_{on} and m is the index number.[24, 25] As shown in **Fig. S9b,c**, $C_{\tau_{off}}$ and $C_{\tau_{on}}$ show an exponential decay with m, suggesting the fluctuations exist in both τ_{off} and τ_{on} reactions. The corresponding correlation time is calculated by multiplying the fitted decay constant (from **Fig. S9b,c**) by the average turnover time (from **Fig. S9a**). Thus, the correlation times for τ_{off} and τ_{on} reactions in **Fig. S9b,c** are calculated to be 6.6 and 1.9 s, respectively. The histogram distributions of correlation times (from > 30 locations) are shown in the insets of **Fig. S9b,c**.

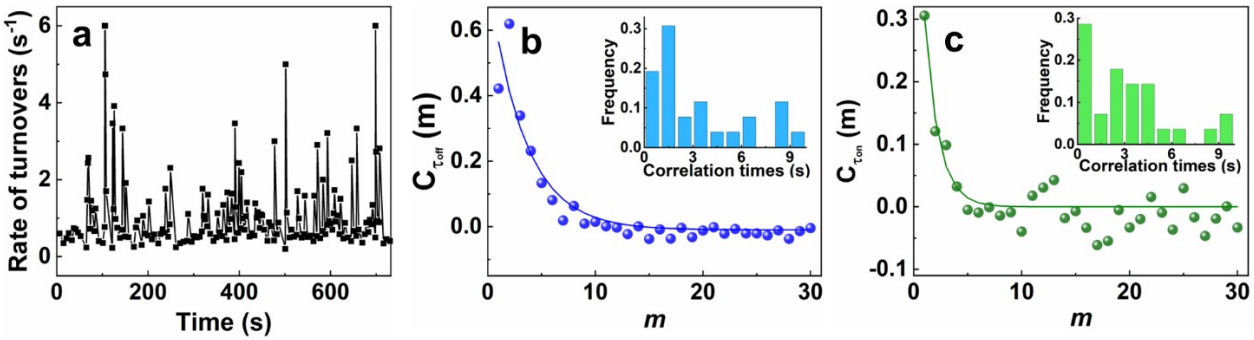

Fig. S9 (a) A single-turnover trajectory from the BP calculated based on every 10 turnovers. Autocorrelation functions of (b) τ_{off} and (c) τ_{on} reactions obtained from (a). Insets: Histogram distribution of correlation times calculated from > 30 subregions.

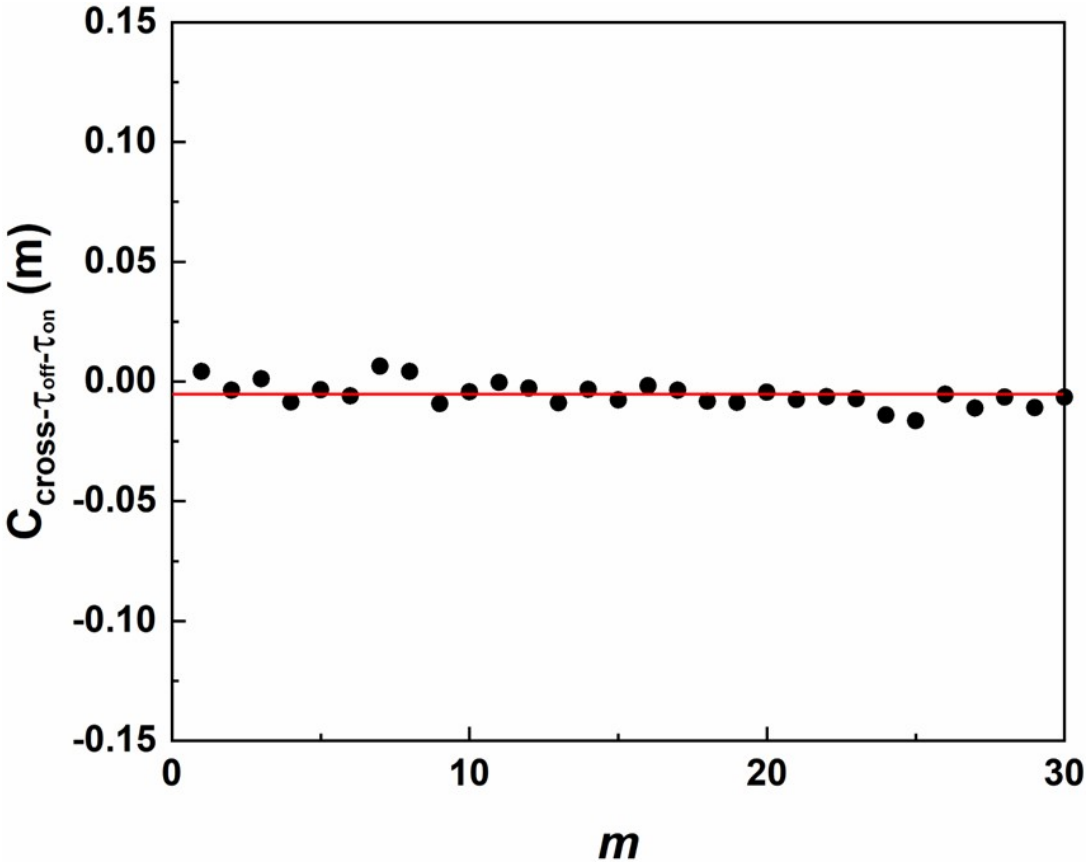

Fig. S10 Cross correlation function of τ_{off} and τ_{on} from the trajectory in **Fig. S9a**.

Section S7. AR adsorption on BP, wrinkle, and edge surfaces by DFT simulation.

In the figures below, the initial and corresponding optimized geometries of AR on different surfaces of g-C_3N_4 are presented in **Fig. S11-S13**. The initial positions of adsorbed species on the surfaces affect the final adsorption geometries as well as the energies, thus we started with nine initial positions to try to cover the most plausible interactions of adsorbate molecule on the surfaces.

We also performed Bader charge analyses to study the change in charge density and quantify the amount of charge transfer between different CNS structures and AR. We found Bader charges of 0.006, 0.036, and 0.013 e to be transferred from AR onto BP, edge, and wrinkle surfaces, respectively. Despite the relatively weaker adsorption energies, there is definite charge transfer from AR to the wrinkle and edge CNS surfaces. As a result, an inbuilt electric field directed from AR to edge and wrinkle is generated at the interface, which enables better separation of photoelectron-hole pairs and enhances photocatalytic activity.[26] More electron transfer observed on the edge and wrinkle indicate better charge separation and faster oxidation of AR on these structures. These electron transfer values are quantitatively low since they are calculated in the ground state; thus, we recommend further material simulations that could unravel the photoactivity of CNS surfaces upon light activation.

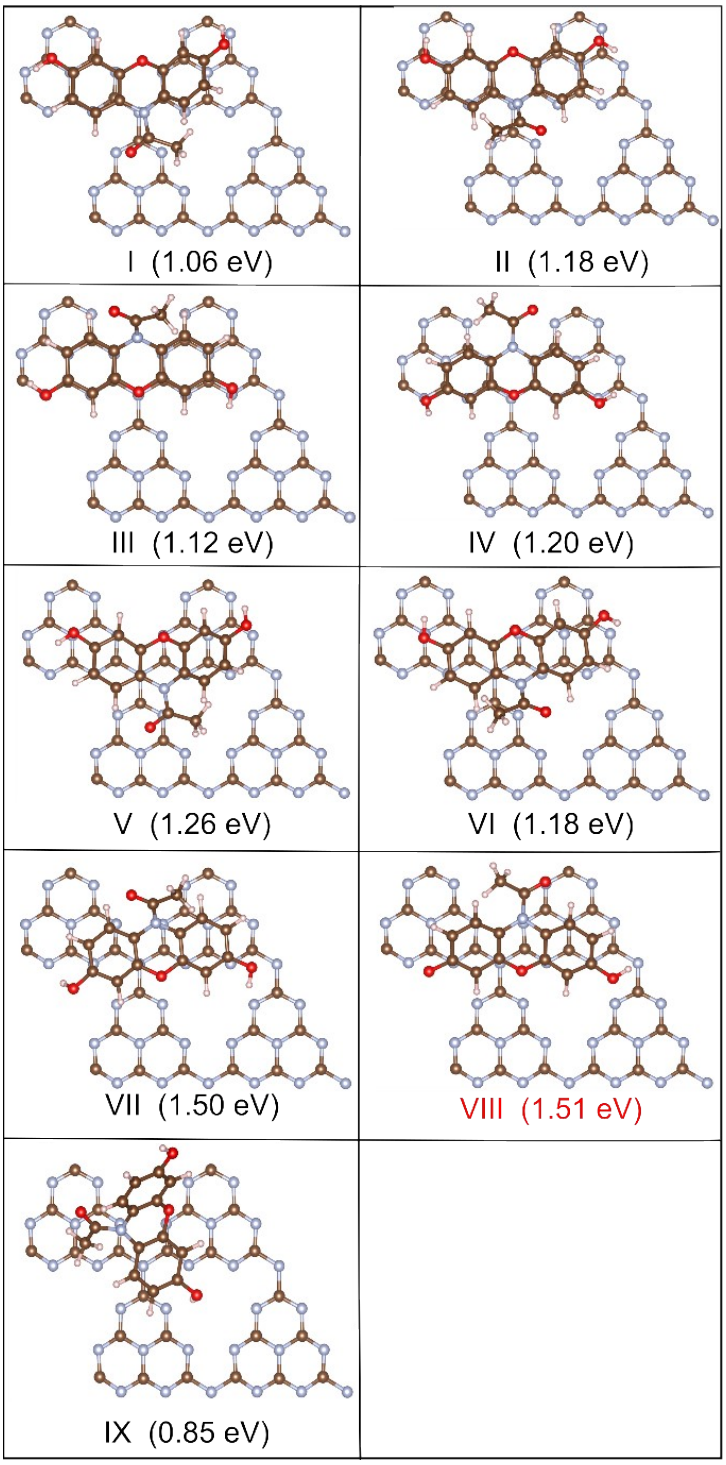

Fig. S11 Optimized geometries of AR on BP surface. Structures I-VIII are flat-on configurations while structure IX is a T-shaped configuration. The most stable structure (VIII) was taken as the final adsorption geometry of AR on BP surface as reported in the manuscript.

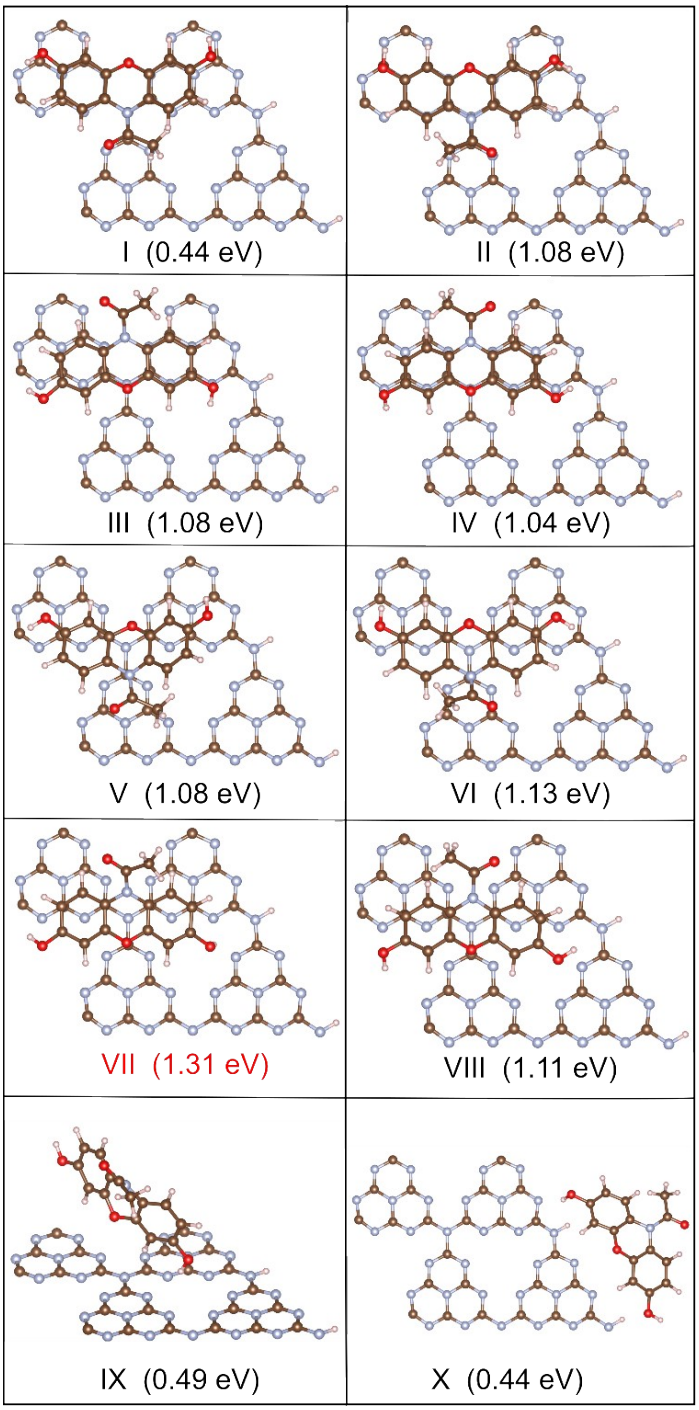

Fig. S12 Optimized geometries of AR on edge surfaces. Structures I-VIII are flat-on configurations while structure IX is an edge-on configuration and X as side configuration. The most stable structure (VII) was taken as the final adsorption geometry of AR on edge surface as reported in the manuscript.

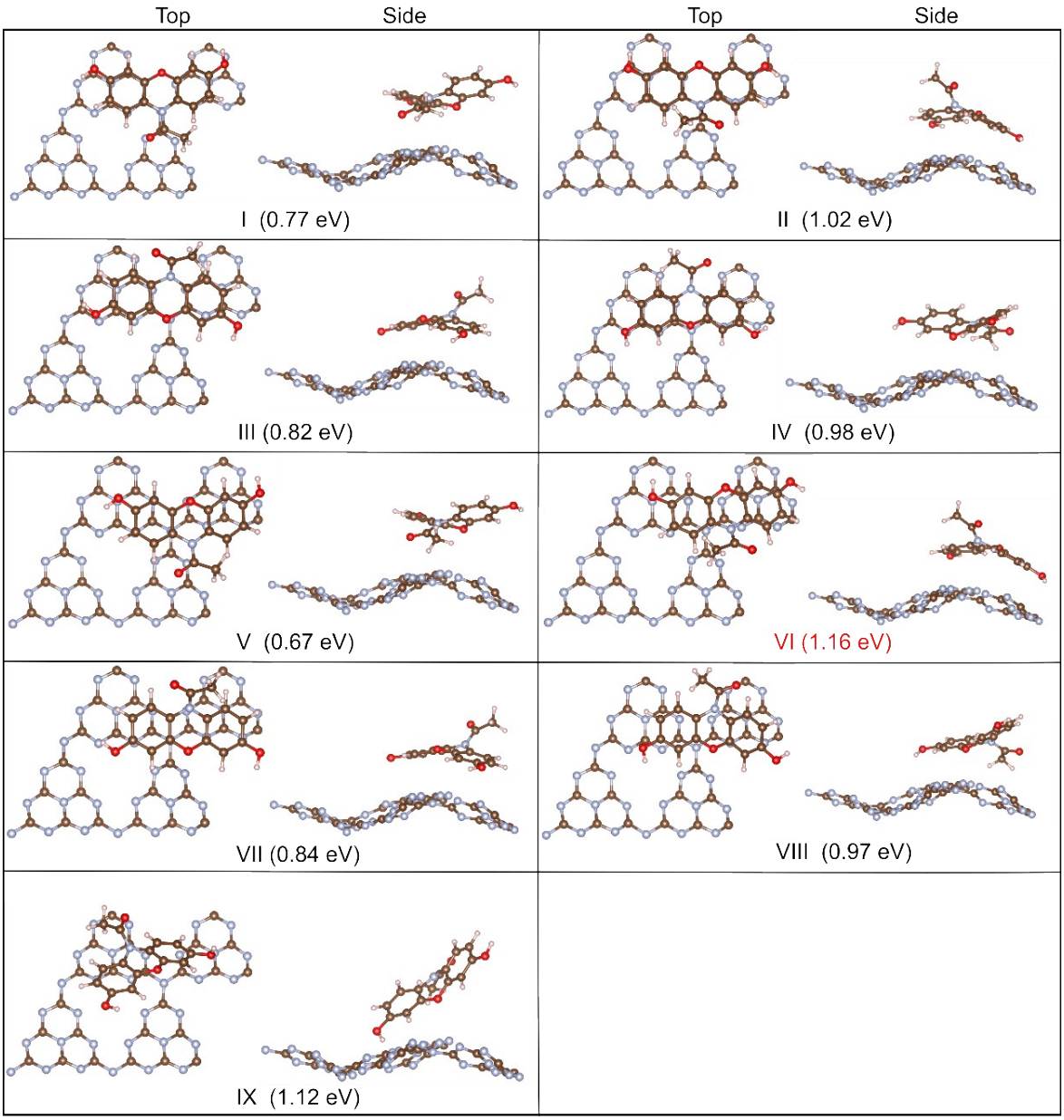

Fig. S13 Optimized geometries of AR on wrinkle surface with top (left) and side (right) views. Structures I-VIII are flat-on configurations while structure IX is an edge-on configuration. The most stable structure (VI) was taken as the final adsorption geometry of AR on wrinkle surface as reported in the manuscript.

Reference

1. Y. Li, R. Jin, Y. Xing, J. Li, S. Song, X. Liu, M. Li and R. Jin, *Adv. Energy Mater.*, 2016, **6**, 1601273.
2. G. Kresse and J. Hafner, *Phys. Rev. B*, 1993, **47**, 558.
3. G. Kresse and J. Hafner, *Phys. Rev. B*, 1994, **49**, 14251.
4. G. Kresse and J. Furthmüller, *Comput. Mater. Sci.*, 1996, **6**, 15-50.
5. G. Kresse and J. Furthmüller, *Phys. Rev. B*, 1996, **54**, 11169.
6. J. P. Perdew, K. Burke and M. Ernzerhof, *Phys. Rev. Lett.*, 1996, **77**, 3865.
7. J. P. Perdew, K. Burke and M. Ernzerhof, *Phys. Rev. Lett.*, 1997, **78**, 1396.
8. P. E. Blöchl, *Phys. Rev. B*, 1994, **50**, 17953.
9. G. Kresse and D. Joubert, *Phys. Rev. B*, 1999, **59**, 1758.
10. S. Grimme, J. Antony, S. Ehrlich and H. Krieg, *J. Chem. Phys.*, 2010, **132**, 154104.
11. S. Grimme, S. Ehrlich and L. Goerigk, *J. Comput. Chem.*, 2011, **32**, 1456-1465.
12. G. Henkelman, A. Arnaldsson and H. Jónsson, *Comput. Mater. Sci.*, 2006, **36**, 354-360.
13. E. Sanville, S. D. Kenny, R. Smith and G. Henkelman, *J. Comput. Chem.*, 2007, **28**, 899-908.
14. W. Tang, E. Sanville and G. Henkelman, *J. Phys. Condens. Matter.*, 2009, **21**, 084204.
15. G. Li, B. Wang, J. Zhang, R. Wang and H. Liu, *Appl. Surf. Sci.*, 2019, **478**, 1056-1064.
16. J. Zhang, J. Chen, Y. Wan, H. Liu, W. Chen, G. Wang and R. Wang, *ACS Appl. Mater. Interfaces*, 2020, **12**, 13805-13812.
17. C. Wu, S. Xue, Z. Qin, M. Nazari, G. Yang, S. Yue, T. Tong, H. Ghasemi, F. C. R. Hernandez and S. Xue, *Appl. Catal. B: Environ.*, 2021, **282**, 119557.
18. P. Niu, L. Zhang, G. Liu and H. M. Cheng, *Adv. Funct. Mater.*, 2012, **22**, 4763-4770.
19. Z. Tong, D. Yang, Y. Sun, Y. Nan and Z. Jiang, *Small*, 2016, **12**, 4093-4101.
20. J. B. Sambur and P. Chen, *J. Phys. Chem. C*, 2016, **120**, 20668-20676.
21. T.-X. Huang, B. Dong, S. L. Filbrun, A. A. Okmi, X. Cheng, M. Yang, N. Mansour, S. Lei and N. Fang, *Sci. Adv.*, 2021, **7**, eabj4452.
22. B. Dong, Y. Pei, F. Zhao, T. W. Goh, Z. Qi, C. Xiao, K. Chen, W. Huang and N. Fang, *Nat. Catal.*, 2018, **1**, 135-140.
23. X. Zhou, W. Xu, G. Liu, D. Panda and P. Chen, *J. Am. Chem. Soc.*, 2010, **132**, 138-146.
24. H. P. Lu, L. Xun and X. S. Xie, *Science*, 1998, **282**, 1877-1882.
25. W. Xu, J. S. Kong and P. Chen, *Phys. Chem. Chem. Phys.*, 2009, **11**, 2767-2778.
26. F. Yu, Z. Wang, S. Zhang, H. Ye, K. Kong, X. Gong, J. Hua and H. Tian, *Adv. Funct. Mater.*, 2018, **28**, 1804512.